

Distribution of Galactic Haloes and their Evolution in Λ CDM Cosmology

Hung-Yu Jian¹ and Tzihong Chiueh^{1,2,3}

hyj@phys.ntu.edu.tw & chiuehth@phys.ntu.edu.tw

ABSTRACT

To investigate the clustering and mass distribution of the overall halo population as well as their evolution, a variant of the hierarchical friends-of-friends algorithm (HFOF) (Klypin et al. 1999), is employed to identify and to locate subhalos. A galaxy formation model is proposed that galaxies can form only in a sufficiently deep gravitational potential so as to facilitate efficient gas cooling. We estimate that such potential is provided by a halo of mass $M \gtrsim M_c \approx 7.30 \times 10^{12} (\Delta_c(z)(1+z)^3)^{-1/2} h^{-1} M_\odot$, where $\Delta_c(z)$ is the mean overdensity of spherically virialized objects formed at redshift z , and $M_c \approx 4.0 \times 10^{11} h^{-1} M_\odot$ at $z = 0$. Our galaxy samples are constructed by selecting subhalos within those FOF halos more massive than M_c . The differential galaxy mass functions of this sample are found to be close to the observation derived from the combination of the luminosity function of the DEEP2 galaxies as well as the mass-to-light ratio from Red-Sequence Cluster Survey at $z = 0.3$. We also analyze the galaxy space density as a function of redshift to examine the density evolution, which is found to be roughly consistent with the observational result based on the luminosity functions in Faber et al. (2007). At $z = 0$, the two point correlation function (CF) of our galaxy sample can be well fitted by a power law down to $\sim 80 h^{-1} kpc$ with an amplitude and slope consistent with those of the SDSS galaxies. The correlation function at $z = 1$ of our sample also agrees with the DEEP2 galaxies. The dependence of the correlation length r_0 and the power index γ on the number density are analyzed. The results that r_0 increases as the number density of galaxies decreases are consistent with observations. In addition, the halo occupation distributions (HODs) of full subhalo samples are compared and found to be consistent with the works of other authors. The HODs

¹Department of Physics, National Taiwan University, 106, Taipei, Taiwan, R.O.C.

²Center for Theoretical Sciences, National Taiwan University, 106, Taipei, Taiwan, R.O.C.

³LeCosPa, National Taiwan University, 106, Taipei, Taiwan, R.O.C.

of our galaxy samples also show good consistency with the SDSS and DEEP2 data. Finally, the kinematic pair fractions for $r_{max} = 50$ and $100 h^{-1} kpc$ are computed, and the evolution is parameterized as $(1+z)^m$. Comparing with the results, $m = 0.41 \pm 0.14$ ($r_{max} = 50$) and $m = 0.29 \pm 0.05$ ($r_{max} = 100$), in Lin et al. (2008), we obtain $m \approx 0.96$ and $m \approx 0.48$ respectively in one of our simulations. Despite steeper slopes, likely caused by our finite mass resolution, the evolutionary trend is still consistent with the observational results.

Subject headings: cosmology: theory — galaxies: formation — galaxies: halos — large-scale structure of universe — methods: numerical

1. Introduction

The standard theoretical model for galaxy formation basically consists of two main elements, the cold dark matter (CDM) model and a dark energy field (which may take the form of a cosmological constant, Λ). The fundamental assumption made in the theory is that structure grew from weak density fluctuations present in the otherwise homogeneous and rapidly expanding early Universe. Afterwards, the gravitational instability drives these fluctuations into nonlinear regime in a bottom up fashion and they gradually grow to a wealth of structures today. Recent diverse cosmological studies, no matter from large-scale structure observations (e.g., Spergel et al. 2003), from supernova data (e.g., Riess et al. 1998), or from light element abundance (e.g., White et al. 1993), all seem to support the concordance model. Due to the highly nonlinear nature in the collapse of fluctuations and the subsequent hierarchical build-up of structure, numerical simulations come to play an indispensable role.

In the past thirty years, galaxy clustering have been intensively studied, as the clustering of galaxies has long been an essential testing ground for various cosmological models and galaxy formation scenarios. Especially due to the advent of modern computers, high resolution simulations become possible. Cosmological N-body simulations have developed into a powerful tool for calculating the gravitational clustering of collisionless dark matter from specified initial conditions. As the resolution of simulations increases, some numerical problems such as the overmerging problem (Klypin et al. 1999) can be overcome, and the galactic size scale in a large scale structure simulation can be resolvable. In addition, the growth of galaxy redshift surveys has led to measurements of increasing precision and detail. All these works have made the comparisons between theories of observations possible.

There are four main approaches used in cosmological simulations to study the galaxy

clustering and properties. The first one is N-body plus hydrodynamical simulation including gas and dark matter particles (e.g., Weinberg et al. 2004). The second method is a hybrid method that combines N-body simulations of the dark matter component with semianalytic treatments of the galaxy formation physics (e.g., Springel et al. 2005). Another approach is using high-resolution collisionless N-body simulations that identify galaxies with "subhalos" in the dark matter distribution (e.g., Klypin et al. 1999; Kravtsov et al. 2004). The last one is the so called Halo Occupation Distribution (HOD) approach which gives a purely statistical description of how dark matter halos are populated with galaxies (e.g., Berlind et al. 2003; Kravtsov et al. 2004; Zheng et al. 2005). It is known that the cold dark matter is the dominant mass component and it interacts only through gravity. To some extent, gravitational dynamics alone should explain the basic features of galaxy clustering. Neyrinck et al. (2004) tried to understand how the infrared-selected galaxies populate dark matter halos, paying special attention to the method of halo identification in simulations. They tested the hypothesis that baryonic physics negligibly affects the distribution of subhalos down to the smallest scales yet observed and successfully reproduced the Point Source Catalogue Redshift (PSCz) power spectrum. Berlind et al. (2003) reported that the HOD prediction of two methods, a semi-analytic model and gasdynamics simulations, agree remarkably well for samples of the same space density. This result indirectly supported the idea that the HOD, and hence galaxy clustering, is driven primarily by gravitational dynamics rather than by processes such as cooling and star formation. On the other hand, Kravtsov et al. (2004) adopt a variant of the bound density maxima (BDM) halo-finding algorithm (Klypin et al. 1999) to identify halos and subhalos and use the maximum circular velocity V_{max} as a proxy of halo mass for selecting galaxy sample. Instead of selecting objects in a given range of V_{max} , at each epoch they selected objects of a set of number densities corresponding to (redshift dependent) thresholds in maximum circular velocity, i.e., $n_i(> V_{max})$. Their results show that the dependence of correlation amplitude on the galaxy number density in their sample is in general agreement with results from the Sloan Digital Sky Survey. In view of these previous works, despite some of our simulations include gas particles, we shall ignore the gas component in the identification of galaxies. Motivated by the results of these previous works, an approach similar to the third one is adopted in this study. Our approach in fact combines a subhalo finding algorithm, HiFOF, plus the galaxy formation model 'directly' locate where the galaxy should be formed and shows an agreement with various observation results, such as galaxy mass function and two-point correlation function. This result indicates that our galaxy identification model can successfully locate subhalos in simulations that reside inside hosting halos in real universe.

The paper is structured as follows. In section 2, we describe the simulation and the halo-finding algorithm in use. Thereafter, the galaxy halo model we adopt is discussed. In

Section 3, we compare our galaxy samples with observations including the differential mass functions, the number density evolution, the correlation functions at different redshift, the halo occupation distribution, and the pair fraction. Finally, we discuss and summarize our results in Sec. 4.

2. Theoretical models

2.1. Simulations

Our simulations have been evolved in the concordance flat Λ CDM model: $\Omega_0 = 0.3$, $\Omega_\Lambda = 0.7$, $\Omega_b = 0.05 h^{-2}$, and $h = 0.66$, where Ω_0 , Ω_Λ , Ω_b are the present-day matter, vacuum, and baryon densities and h is the dimensionless Hubble constant defined as $H_0 \equiv 100 h \text{ km s}^{-1} \text{ Mpc}^{-1}$. These parameters are consistent with current observations on cosmological parameters (Spergel et al. 2003; Tegmark et al. 2004; Seljak et al. 2005; Sanchez et al. 2006) with $\Omega_{dm} = 0.20 \pm 0.020$, $\Omega_b = 0.042 \pm 0.002$, $\Omega_\Lambda = 0.76 \pm 0.020$, $h = 0.74 \pm 0.02$. Four realizations with different box sizes and particle numbers were analyzed and compared to investigate the boundary and resolution effects as well as to have better statistics. GADGET1 (Springel et al. 2001b) and GADGET2 (Springel 2005) were both employed to conduct the simulations. Our simulations all started at redshift $z = 100$ and evolved to $z = 0$, and their density spectra were normalized to $\sigma_8 = 0.94$, where σ_8 is the rms fluctuation in sphere of $8 h^{-1} \text{ Mpc}$ comoving radius. The first simulation (ΛCDM_{100a}) follows the evolution of 256^3 dark matter particles and 256^3 gas particles in a $100 h^{-1} \text{ Mpc}$ box on a side. The mass of a dark matter particle is $m_{dm} = 4.125 \times 10^9 h^{-1} M_\odot$, while the mass of a gas particle is $m_{gas} = 8.25 \times 10^8 h^{-1} M_\odot$. In addition, We adopted a softening length switching from a comoving scale to a physical scale at $z = 2.3$. The softening length ϵ was $20 h^{-1} \text{ kpc}$ (comoving) before redshfit $z = 2.3$. After that, ϵ was switched to $6 h^{-1} \text{ kpc}$ (physical). Thus, the highest force resolution is $6 h^{-1} \text{ kpc}$. The second simulation (ΛCDM_{200}) follows the evolution of 512^3 dark matter particles and 512^3 gas particles in the same cosmology but in a $200 h^{-1} \text{ Mpc}$ box on a side. Both dark matter particles and gas particles have the same masses respectively as in the first simulation, but in this run ϵ keeps constant at $10 h^{-1} \text{ kpc}$ (comoving). The third simulation (ΛCDM_{100b}) evolves 512^3 pure dark matter particles in a $100 h^{-1} \text{ Mpc}$ box on a side. The mass of a dark matter particle is $m_{dm} = 6.188 \times 10^8 h^{-1} M_\odot$. We also adopt a softening length switching scheme in this simulation. However, the softening length ϵ was set to be $10 h^{-1} \text{ kpc}$ (comoving) before redshfit $z = 2.3$ and was modified to $3 h^{-1} \text{ kpc}$ (physical) thereafter. The final simulation (ΛCDM_{100c}) was run with 512^3 dark matter particles and 512^3 gas particles in a $100 h^{-1} \text{ Mpc}$ box on a side, and $m_{dm} = 5.156 \times 10^8 h^{-1} M_\odot$, $m_{gas} = 1.031 \times 10^8 h^{-1} M_\odot$, and ϵ was kept constant at $10 h^{-1} \text{ kpc}$ (comoving). The parameters of

our simulations are summarized in Table 1.

2.2. Hierarchical Friends-of-Friends Algorithm (HiFOF)

There are many widely used algorithms for identifying the substructures, such as Bound Density Maxima (BDM ; Klypin et al. 1999), SKID (Stadel et al. 1997), and subfind (Springel et al. 2001a). These methods were developed to overcome the problem of identification of dark matter halos in the very high density environments in groups and clusters. We use a variant of Hierarchical Friends-of-Friends Algorithm (HFOF ; Klypin et al. 1999) for the halo substructure identification. To distinguish from HFOF, we call our method HiFOF.

The Friends-of-Friends (FOF; see, e.g., Davis et al. 1985) algorithm as a base of HiFoF identifies virialized cluster halos by using a linking length of $0.2 \bar{l}$ to link particles as a group if the separation of two particles are shorter than the linking length; here, $\bar{l} = n_0^{-1/3}$ and n_0 is the mean particle density in the simulation box. However, FOF is not capable of finding substructures in cluster halos. Our algorithm, HiFOF, applies the FOF algorithm with a hierarchical set of linking lengths plus a virial condition check on all identified groups on all level. The detail description for HiFOF is as follows. We construct sixteen hierarchical levels by decreasing progressively from the linking length $0.2 \bar{l}$, the lowest level, to $0.04 \bar{l}$, the highest level. Because of different mass resolution in our simulations, we setup up two different criterions for the minimum particle number allowed for a group. In the ΛCDM_{100a} and the ΛCDM_{200} , the minimum particle number for a group searched is set to be ten, $n_{min} \geq 10$, corresponding $4.1 \times 10^{10} h^{-1} M_\odot$. As in the ΛCDM_{100b} and the ΛCDM_{100c} , n_{min} is set to be greater than 30, corresponding to $1.9 \times 10^{10} h^{-1} M_\odot$ and $1.55 \times 10^{10} h^{-1} M_\odot$, respectively. To examine the resolution effect due to n_{min} , the analysis in ΛCDM_{100c} with $n_{min} = 10$, corresponding to $5.15 \times 10^9 h^{-1} M_\odot$, is additionally included and marked $^*\Lambda\text{CDM}_{100c}$. During the hierarchical tree construction, any group with particle number less than n_{min} is discarded. For every cluster halo, once a tree of sixteen levels are built, a virial condition check is then performed on every member in the tree. The virial condition is calculated by summing up the potential energy and kinetic energy in physical coordinates of all particles in a group. A parameter for the virial condition check is defined as

$$\beta = 2 \frac{\sum_i E_{kinetic}(i)}{\sum_i E_{potential}(i)} - 1 \quad (1)$$

where i sums over the entire particles in a subhalo. It is known that for a virialized system the virial parameter β is greater than 0. However, the virial condition for subhalos within a halo

could be made less restrictive due to the potential well of the subhalo inside a deeper halo potential. Nevertheless, it is difficult and impractical to really calculate the extra potential energy provided by the cluster or group halo. We therefore adopt a loose constraint that β has to be greater than -3; that is, we allow a group with $E_{kinetic} \leq 2|E_{potential}|$ to pass the virial condition. The samples adopting this loose constraint turn out to do better in the comparisons with observations than the ones adopting the original condition, $\beta = 0$.

Additionally, unlike the unbound procedure that iteratively removes the unbound particles with the greatest total energy until only bound particles remain in the subhalo (Springel et al. 2001a), our subhalos are treated as a whole and can not be separated into bound and unbound particles. In other words, if a subhalo can not pass the virial condition check, we will drop it entirely. After the virial conditions of all subhalos in the tree are checked, the virialized subhalos on every branch at the highest possible level are then selected to be the samples used in our analysis; other unvirialized subhalos and virialized subhalos not at the highest possible level are dropped. Figure 1 schematically shows how the HiFOF algorithm works. Continuing the same procedure on all FOF halos, subhalo samples are then constructed. This full subhalo sample is also called the HiFOF sample in this study.

Figure 2 shows the cumulative mass functions of subhalos for the four simulations at redshifts $z = 0$ (left) at $z = 1$ (right). The densities are $7.11 \times 10^{-2} h^3 Mpc^{-3}$ (ΛCDM_{100a}), $7.33 \times 10^{-2} h^3 Mpc^{-3}$ (ΛCDM_{200}), $1.53 \times 10^{-1} h^3 Mpc^{-3}$ (ΛCDM_{100b}), $1.53 \times 10^{-1} h^3 Mpc^{-3}$ (ΛCDM_{100c}), and $4.37 \times 10^{-1} h^3 Mpc^{-3}$ ($*\Lambda CDM_{100c}$) at $z = 0$. The accumulated subhalo mass functions in our simulations basically are consistent with each other. In other words, at the same redshift the mass function is mildly dependent on the box size and the mass resolution. However, it is observed that the rapid increase appears at low mass end and is possibly due to the resolution effect if two different resolution runs are compared. At $z = 1$, the four simulations agree with each other to a lesser degree. It is indicated that the difference likely arises from the different softening-length adoption as well as from sample variance.

2.3. Galaxy Model

Galaxy formation involves complicated processes. Despite that, cooling is essential to lower the specific entropy in the gas, thereby increasing the gas density. Bremsstrahlung cooling is the most efficient cooling mechanism for this purpose. However, it requires the gas to exceed the ionization temperature. As a self-gravitating gas is cooled by Bremsstrahlung, the gas can be heated by adiabatic contraction, where it is possible for the gas to maintain a temperature above ionization, thereby leading to cooling runaway. Hence in our galaxy

model, we demand that the host halo potential must be sufficiently deep for the gas to get above the ionization temperature. This condition is translated to a threshold host halo mass, only above which the galaxy can form within such a host halo.

Now, consider a halo with a virial mass M and a virial radius R , M can be related to R as

$$M = \frac{4\pi}{3}\rho_{vir}R^3 = \frac{4\pi}{3}\Delta_c(z)\rho_{bg}R^3, \quad (2)$$

where ρ_{vir} is the virial density, $\Delta_c(z)$ the mean overdensity of spherically virialized objects formed at redshift z , and ρ_{bg} the background density $\equiv \rho_0(1+z)^3$. The overdensity $\Delta_c(z)$ at each redshift can be computed using a fitting formula by Kitayama & Suto (1996). For example, $\Delta_c \approx 335$ at $z = 0$ and $\Delta_c \approx 201$ at $z = 1$ for our cosmology, $\Omega_0 = 0.3$ and $\Omega_\Lambda = 0.7$.

In order to facilitate efficient gas cooling, a deep gravitational potential is needed for the virial temperature to exceed the ionization temperature, i.e. $kT_{vir} \gtrsim \frac{1}{2}\alpha^2 m_e c^2$, where α is the fine structure constant, m_e the electron mass, and c the speed of light. The high-temperature virial temperature for a halo can be obtained as

$$kT_{vir} \approx \frac{GMm_p}{5R} \gtrsim \frac{1}{2}\alpha^2 m_e c^2 \quad (3)$$

where G is the gravitational constant, k the Boltzmann constant, and m_p the proton mass. Using Eq. (2) to replace R by M , it follows that

$$M \gtrsim M_c \approx \left(\frac{(\frac{5}{2}(\frac{3}{4\pi})^{1/3}\alpha^2 m_e c^2)}{(\Delta_c(z)\rho_{bg})^{1/3}Gm_p} \right)^{3/2} \approx 7.30 \times 10^{12} (\Delta_c(z)(1+z)^3)^{-1/2} h^{-1} M_\odot. \quad (4)$$

At $z = 0$, the threshold halo mass $M_c \approx 4.0 \times 10^{11} h^{-1} M_\odot$. We apply the mass cut to select those FOF halos, which host our galaxy samples.

3. Simulation Results and Observations

In this section we will compare our galaxy samples with the observed galaxies. Comparisons include the differential mass function, the galaxy number density evolution, the two point correlation function at low and high redshifts, the halo occupation distribution, and finally the kinetic pair fraction.

3.1. Differential Mass Function

Luminosity function (LF for short) $\phi(L)$ gives the relative numbers of galaxies of different luminosities, and is so defined that $\phi(L)dL$ is the number of galaxies in the luminosity interval $L \rightarrow L + dL$ per unit volume of the Universe. The luminosity function of galaxies can be fitted by Schechter’s (1976) formula,

$$\phi(L)dL = \phi^* \left(\frac{L}{L_*}\right)^\alpha \exp\left(-\frac{L}{L_*}\right) \frac{dL}{L_*}. \quad (5)$$

We adopt $\phi^* = (26.39_{-1.62}^{+1.81}) \times 10^{-4} \text{ Mpc}^{-3}$, $\alpha = -1.30$, and $L_* = 10^{((M^*+M_{\odot B})/2.5)} L_{\odot} = 1.987 \pm 0.25 \times 10^{10} L_{\odot}$ for $M^* = -21.07 \pm 0.13$ from DEEP2 B-band galaxies at $z \sim 0.3$ (Faber et al. 2007) for comparison later in our analysis. The mass function and luminosity function have a relation that $F(M)dM = \phi(L)dL$. If L can be expressed as a function of M , $F(M)$ can be derived. Hoekstra et al. (2005) measured the weak-lensing signal as a function of rest-frame B-, V-, and R-band luminosities for a sample of “isolated” galaxies from the Red-Sequence Cluster Survey with photometric redshifts $0.2 < z < 0.4$. They fit the measurements with a power-law form for the mass-to-light ratio

$$M = M_{fid} \left(\frac{L}{10^{10} h^{-2} L_{\odot}}\right)^\beta, \quad (6)$$

where M_{fid} is the virial mass of a fiducial galaxy of luminosity $L = 10^{10} h^{-2} L_{x,\odot}$, where x indicates the relevant filter. In B band, they obtained $M_{fid} = 9.9_{-1.3}^{+1.5} \times 10^{11} h^{-1} M_{\odot}$ and $\beta = 1.5 \pm 0.3$. With the power law form of the mass-to-light ratio, $F(M)$ can be computed as follows,

$$F(M) = \frac{\phi^*(10^{10})^{\alpha+1}}{L_*^{\alpha+1} \beta M_{fid}} \times \left(\frac{M}{M_{fid}}\right)^{\frac{\alpha+1}{\beta}-1} \times \exp^{-\left(\frac{M}{M_{fid}}\right)^{1/\beta} \frac{10^{10}}{L_*}}. \quad (7)$$

However, the galaxy mass measured by the weak lensing signal is in fact an overestimate, as the lensing signal is mostly produced by the halo surrounding the subhalo, instead of by the subhalo itself. In order to make a fair comparison between the observations and our simulations, we search halos in our simulations with only one HiFOF subhalo resides in an FOF halo, i.e. the isolated galaxy, and plot the relation between the FOF halo mass and the subhalo mass. The result is shown in Figure 3. It is found that the relation reveals a power-law form. We shall therefore apply this relation to our galaxy samples.

Figure 4 shows differential mass functions of the LF + M/L obtained in Eq. (7) and our galaxy samples at $z = 0.3$ after applying the $M_g - M_h$ relation in Fig. 3 to our galaxy samples. The mass functions of four simulations agree with the observation as well as with each other quite well. In highest mass range, $M > 10^{13} h^{-1} M_\odot$, and in the low mass end, the profiles of our mass functions show the excess compared with the observational data. In the ΛCDM_{100c} and $^*\Lambda\text{CDM}_{100c}$ simulation, respectively with $n_{min} = 30$ and $n_{min} = 10$, it can be observed that the excess at low-mass end with the high resolution is pushed to lower galaxy mass than with the low one. Hence, it is inferred that the low-mass excess is likely caused by the insufficient mass resolution. As for the high-mass excess, it is probably related to over-abundance of CD galaxies at the cluster centers, whose population deviates from the Schechter’s function.

3.2. Galaxy Density Evolution

As the high redshift data are gradually collected by observations in recent years, study of galaxy properties in time evolution becomes feasible. An aspect to examine our galaxy model is to make comparison with the observed galaxy density evolution. When we integrate Eq. (5) over luminosity, it gives the galaxy number density,

$$n_{(>L)} = \int_L^\infty \Phi(L') dL'. \quad (8)$$

That is, with given ϕ^* , α , L_* , and a luminosity cut L , the galaxy number density can be known through the integration. It’s indicated in Conroy et al. (2005) that isolated galaxies at $z \sim 1$ have a similar halo mass as isolated galaxies that are 1 mag fainter at $z \sim 0$. They found that there has been little or no evolution in the halo mass of isolated galaxies with magnitudes in the range $\sim M_B^* - 0.5$ to -1.5 , even though M_B^* has evolved by ~ 1 mag over this redshift range. This result is adopted in our analysis, but it is assumed that there is no evolution of isolated galaxies even with magnitudes $\sim M_B^* + 2.5 \log_{10} 4$, which is equivalent to $L_*/4$. The luminosity cut L in Eq. (8) for $n_{(>L)}$ is manually set to be greater than $L_*(z)/4$. That is, the cut is $L_*(z)$ -dependent. In contrast, our simulations need to find the corresponding redshift-independent mass-cut to make a right comparison if the previous result and the assumption are adopted. Unlike other people using galaxy density corresponding to the certain absolute magnitude thresholds to determine the galaxy mass, we take a different approach that combines the LF of the DEEP2 B-band galaxies and the mass-to-light relation at $z \sim 0.3$, as well as the $M_g - M_h$ relation discussed in Section 3.1 to obtain the corresponding mass-cut. The luminosity cut of $L_*(z \sim 0.3)/4$ given from the result of the observed DEEP2 LF is then converted to a galaxy mass-cut in our samples with

$7.02 \times 10^{10} h^{-1} M_{\odot}$ in the ΛCDM_{100a} , $7.06 \times 10^{10} h^{-1} M_{\odot}$ in the ΛCDM_{200} , $7.01 \times 10^{10} h^{-1} M_{\odot}$ in the ΛCDM_{100b} , $6.66 \times 10^{10} h^{-1} M_{\odot}$ in the ΛCDM_{100c} , and $5.79 \times 10^{10} h^{-1} M_{\odot}$ in the $^*\Lambda\text{CDM}_{100c}$. The mass cut is applied to all redshift and the redshift evolution of the galaxy number density is then obtained in our galaxy samples.

Figure 5 presents the number density evolution of our data and the observed galaxy density data by integrating the luminosity functions (Eq. 8) in Faber et al. (2007) which include measurements of Combo-17 (Faber et al. 2007), FDF (Gabasch et al. 2004), Bell SDSS (Bell et al. 2003), VVDS (Ilbert et al. 2005), 2df (Norberg et al. 2002), DEEP2 (Faber et al. 2007), and SDSS (Blanton et al. 2003). The profiles of our galaxy density basically are in broad agreement with the observed galaxies. Our data show the same evolutionary trend, a decline with the redshift, consistent with the observational data. However, at low redshift, a depletion is found in our simulations. The depletion probably can be attributed to the failure of the assumption at low redshift about the redshift-independent mass-cut, and can be supplemented if a different mass-cut at low redshift is assumed.

3.3. Two-Point Correlation Function

The two-point correlation function $\xi(r)$ (CF for short) is the most used indicator to quantify the degree of clustering in a galaxy sample. It is defined as a measure of the excess probability above Poisson for finding an objects in a volume element dV at a separation r from an otherwise randomly chosen object,

$$dP = n[1 + \xi(r)]dV, \quad (9)$$

where n is the mean number density of the object in question. It has a very simple form of power law,

$$\xi(r) = \left(\frac{r}{r_0}\right)^{-\gamma}, \quad (10)$$

where r_0 is the correlation length and γ is the power index of CF.

Two point correlation functions of our galaxy samples at $z = 0$ are shown in Figure 6 (top). The solid line with error bars represents the full flux-limited sample ($14.5 \leq r \leq 17.77$) of SDSS galaxy (Zehavi et al. 2005) with $r_0 = 5.94 \pm 0.05 h^{-1} Mpc$ and $\gamma = 1.79 \pm 0.01$. The error bars shown in our simulations for the CF are the errors around the mean, estimated from jackknife resampling using the eight octants of the simulation cube (see Weinberg et al. 2004). We take an additional galaxy mass cut on our galaxy samples where $M_g \geq 4.1 \times$

$10^{10} h^{-1} M_{\odot}$ corresponding to a minimum of 10 particles in the ΛCMD_{100a} and ΛCMD_{200} , 66 particles in ΛCMD_{100b} , and 80 particles in ΛCMD_{100c} . After the cut, the galaxy densities become $1.71 \times 10^{-2} h^3 \text{ Mpc}^{-3}$ in ΛCDM_{100b} and $1.24 \times 10^{-2} h^3 \text{ Mpc}^{-3}$ in ΛCDM_{100c} . Our CFs are fit as power laws over the range of scales from 0.1 to $13 h^{-1} \text{ Mpc}$. The correlation lengths in the ΛCDM_{100a} , ΛCDM_{200} , ΛCDM_{100b} , and ΛCDM_{100c} are $5.50 \pm 0.29 h^{-1} \text{ Mpc}$, $5.01 \pm 0.12 h^{-1} \text{ Mpc}$, $6.00 \pm 0.38 h^{-1} \text{ Mpc}$, and $5.56 \pm 0.19 h^{-1} \text{ Mpc}$, and the power indices 1.83 ± 0.04 , 1.80 ± 0.02 , 1.76 ± 0.05 , and 1.70 ± 0.02 , respectively. Both the amplitude and shape of the CF at $z = 0$ are in good agreement with those of the SDSS data. The close agreement of galaxy correlation functions implies that the overall clustering of the galaxy population is determined by the distribution of their dark matter subhalos plus the requirement of a sufficiently deep halo potential to trigger galaxy formation. In Fig. 6 we also plot the subhalo-subhalo correlation ξ_{hh} without the additional requirement of a sufficiently deep subhalo potential. It is clearly noted that ξ_{hh} also obeys a power law form, but with a smaller index, $\gamma \sim 1.4$, and a comparable correlation length $r_0 \sim 5.4 h^{-1} \text{ Mpc}$ in the ΛCDM_{100b} and ΛCDM_{100c} as well as a smaller correlation length $r_0 \sim 3.5 h^{-1} \text{ Mpc}$ in the ΛCDM_{100a} and ΛCDM_{200} . The bias $b(r)$ values shown in Fig. 6 (bottom) display an antibias in the range between $100 h^{-1} \text{ kpc} < r < 2 h^{-1} \text{ Mpc}$ similar with the results in Kravtsov et al. (2004). On the other hand, the deviation of the bias values at $r < 100 h^{-1} \text{ kpc}$ is mainly caused by the difference in ξ_{mm} .

Figure 7 shows the results of the projected correlation functions,

$$w_p(r_p) = \int_0^{r_{max}} \xi(\sqrt{r_p^2 + z^2}) dz \quad (11)$$

at $z = 1$ of our galaxy samples for the four simulations and the volume-limited sample of bright (corrected), $M_B \geq -19.0$, DEEP2 galaxies (Coil et al. 2006). The upper integration limit is set to $r_{max} = 25 h^{-1} \text{ Mpc}$ in our simulations. The DEEP2 galaxy sample has a density of $1.3 \times 10^{-2} h^3 \text{ Mpc}^{-3}$. We therefore select our samples to match the density of the DEEP2 sample by limiting our galaxy samples beyond a certain mass threshold. In Figure 7, it can be seen that the correlation functions of the DEEP2 galaxies and our samples also agree quite well.

In Figure 8 and Figure 9, the correlation length r_0 and the power index γ are plotted as a function of different space density at $z = 0$ and $z = 1$, respectively. The CFs are fit over the range of scales from 0.2 to $13 h^{-1} \text{ Mpc}$. Figure 8 is basically adopted from Fig. 11 in Kravtsov et al. (2004) which includes the Two-Degree Field (2dF; Norberg et al. 2002), SDSS galaxy surveys (Zehavi et al. 2002; Budavari et al. 2003) and their simulation data. We additionally add the newest SDSS data (Zehavi et al. 2005) and our galaxy data into Fig. 8. The strong dependence of correlation length r_0 on the number density n is evident in Figure 8. That is, brighter galaxies are more clustered. In addition, a nearly constant profile

of γ in observations is seen. The amplitude of γ in our simulations, in general, also presents a roughly flat trend although at $n \approx 10^{-2} h^3 \text{ Mpc}^{-3}$ our n values have slight depletion compared with the observations. At $z = 1$ we plot the DEEP2 data released by Coil et al. (2006), the simulation results of Kravtsov et al. (2004), and our data. A similar conclusion as at $z = 0$ is obtained for r_0 , and the values of γ show good consistency with the DEEP2 galaxies. The low γ value in ΛCDM_{100a} compared to the other three simulations likely results from sample variance. Both our correlation length r_0 and power index γ show fair consistency with the observational data in both the values and the trend, in that the smaller the density, the larger the correlation length.

3.4. Halo Occupation Distribution (HOD)

This section will be divided into two sub-sections. In the first sub-section, the HODs of HiFOF samples are analyzed and some results are discussed. Thereafter, the HODs of our galaxy samples are compared with that of the observational data.

3.4.1. the HOD of HiFOF Samples

The HOD formalism, developed during the last several years, has become a powerful theoretical framework for predicting and interpreting galaxy clustering. The original HOD uses the probability $P(N|M)$ to describe the bias of a class of galaxies that a halo of virial mass M contains N such galaxies. Berlind et al. (2003) studied HOD and found that at a given halo mass it is statistically independent of the halos large-scale environment. In addition, they compared HOD of a semianalytic model and gasdynamics simulations in detail and concluded that their HOD predictions for samples of the same space density agree remarkably well despite the two methods predict different galaxy mass functions.

Kravtsov et al. (2004) showed that HOD can actually be understood as a combination of the probability for a halo of mass M to host a central galaxy and the probability to host a number of satellite galaxies that obeys Poisson statistics. We analyze the first moment of HOD, $\langle N(M_h) \rangle \equiv \langle N_c(M_h) \rangle + \langle N_s(M_h) \rangle$, as a function of host mass M_h for the halo samples, where $\langle N_c \rangle$ is the HOD of central galaxies modeled as a step function $\langle N_c \rangle = 1$ with $\langle N_c \rangle = 0$ for $M < M_{min}$ and $\langle N_s \rangle$ the satellite galaxies model as a power law $\langle N_s \rangle \propto M^\beta$ suggested by Kravtsov et al. (2004). Seen from Figure 10 is that the shape of $\langle N(M_h) \rangle$ (solid line) is complicated, but $\langle N_s \rangle$ (plus points) indeed shows a nearly power-law form over three to four orders of magnitude. The α parameter (the upper part in a panel), a convenient measure of

how different $P(N|M)$ is from the Poisson distribution, defined as

$$\alpha \equiv \frac{\langle N(N-1) \rangle}{\langle N \rangle^2}, \quad (12)$$

is evaluated for different distributions including the full HOD, the satellite HOD with $\langle N_s \rangle = \langle N \rangle - 1$, the nearest integer distribution with $N_l \leq \langle N \rangle < N_l + 1$ (where N_l is an integer), and $1 - \frac{1}{\langle N \rangle^2}$ which can be derived from α if a satellite HOD is assumed a Poisson distribution. Additionally, it is known that if the distribution is Poisson, $\alpha = 1$. At high mass range, both the satellite HOD and the full HOD are close to Poisson distribution but they turn to sub-Poisson when the host mass is near the minimum halo mass. However, the satellite HOD remains close to Poisson distribution down to masses an order of magnitude smaller than that for the full HOD. Moreover, α for the full HOD is very similar to the profile of $1 - \frac{1}{\langle N \rangle^2}$, showing that the satellite HODs indeed very close to Poisson distribution. It also can be observed that distribution of the full HODs near M_{min} are close to the nearest integer distribution. These results are consistent with those concluded by Kravtsov et al. (2004).

The satellite HOD was parameterized in Kravtsov et al. (2004) as

$$\langle N_s \rangle = \left(\frac{M}{M_1} - C \right)^\beta, \quad (13)$$

where M_1 is the normalization, defined as $\langle N_s(M_1) \rangle = 1$, and C is a redshift dependent parameter to define the minimum halo mass $M_{min} = CM_1$ such that $\langle N_s \rangle$ approaches zero near $M \sim M_{min}$. Table 2 lists the results of the best-fit parameters M_1 , β , and C for the four simulations at $z = 0$ and at $z = 1$, respectively. From the table, it is seen that the fitting parameters are similar in the ΛCDM_{100a} and ΛCDM_{200} runs. In the ΛCDM_{100b} and ΛCDM_{100c} runs, we also observe the same conclusion. In other words, the box size has little effect on HODs with the same number density. Moreover, the parameter M_{min} evolves with the number density of the samples if we compare ΛCDM_{100a} and ΛCDM_{100b} . It is also seen in the table that parameters M_1 , β , and M_{min} appear mild evolution with redshift. However, our slopes, $\beta \approx 0.7$, are slightly shallower than those reported by Kravtsov et al. (2004), where the $\beta \approx 1$.

Figure 11 displays a comparison of $\langle N_s \rangle$ at two different epochs. The mass is in units of the minimum mass of the sample, M_{min} . At $z = 0$, the number density is reported in Sec. 2.2, whereas at $z = 1$, $n = 8.16 \times 10^{-2} h^3 \text{ Mpc}^{-3}$ in ΛCDM_{100a} , $n = 8.48 \times 10^{-2} h^3 \text{ Mpc}^{-3}$ in ΛCDM_{200} , $n = 1.81 \times 10^{-1} h^3 \text{ Mpc}^{-3}$ in ΛCDM_{100b} , $n = 1.81 \times 10^{-1} h^3 \text{ Mpc}^{-3}$ in ΛCDM_{100c} , and $n = 5.34 \times 10^{-1} h^3 \text{ Mpc}^{-3}$ in $^*\Lambda\text{CDM}_{100c}$. At both epochs, the satellite HODs in the four simulations are in good agreement. Thus, the effects of the box size, the mass resolution and the number density are not prominent. In addition, weak evolution with time in $\langle N_s \rangle$ is seen in Fig. 11 as well.

3.4.2. Comparisons of the HOD between our galaxy samples and the observations

It is discussed in previous sub-section that Kravtsov et al. (2004) modeled $\langle N \rangle$ of a HOD as a combination of central and satellite objects. Zehavi et al. (2005) used this HOD framework to interpret their results. Due to a limited (but important) subset of information encoded in the correlation function for galaxy clustering, a restricted HOD model was fitted with a small number of free parameters, given a underlying cosmological model. The HOD formulation they implemented has three free parameters: M_{min} , the minimum halo mass for galaxies above the luminosity threshold, M_1 , the mass of a halo hosting one satellite galaxy above the luminosity threshold, and α , the power law slope of the satellite mean occupation function. They took M_{min} to be fixed by matching the observed space density of the sample, leaving M_1 and α as free parameters to fit their projected CFs. Moreover, Zheng et al. (2007) modeled the luminosity-dependent projected two-point correlation function of DEEP2 ($z \sim 1$) and SDSS ($z \sim 0$) galaxies within the HOD framework. They adopted a slightly more flexible parameterizations with five parameters, motivated by the results presented in Zheng et al. (2005) as well as with three parameter parameterizations. Only their three parameter results are adopted in our analysis.

We compute the HOD of our galaxy samples to obtain M_{min} , M_1 , and α as a function of galaxy number density to make comparisons with SDSS and DEEP2 galaxies. In Figure 12(a), from top to bottom, our results of M_{min} , M_1 , and α in the four simulations at $z = 0$ and these of SDSS galaxies are compared. It can be seen that M_{min} and M_1 of four simulations not only agree with each other, implying the lesser degree of dependence on the box size and the resolution, but also match the observation quite well no matter in the magnitude or the trend. Despite the increasing trend of the slope α with a decreasing density similar to that of SDSS galaxies, the α value of our HODs on the whole appears to be slightly smaller than that of the observations. This may results from insufficient subhalos found in massive clusters. Fig. 12(b) shows our results at $z = 1$ and the observational data of DEEP2 galaxies. It can be observed that agreements on M_{min} , M_1 , and α are good.

3.5. Pair Fraction

As our galaxy sample can well reproduce the observed evolution of galaxy number density, the mass function, the HOD and the 2-point correlation function, we therefore attempt to test the limit of the sample by exploring the pair fraction and merger rate.

DEEP2 Team (Lin et al. 2004) explored the kinematic close pair fraction and merger rate up to redshift $z \sim 1.2$ and disclosed weak evolution in the galaxy pair fraction. Assuming

mild luminosity evolution, they found the number of companions per luminous galaxy to evolve as $(1+z)^m$, with $m = 0.51 \pm 0.28$ for the $r_{max} = 50 h^{-1} kpc$ case. Recently, (Lin et al. 2008) use more complete data to study the same problem again, and obtain a improved result with $m = 0.41 \pm 0.20$ for all galaxies. These two studies consistently reveal that the pair fraction of galaxies indeed undergo weak evolution. We study the pair fraction problem with our galaxy samples; our approach is in contrast to applying a "hybrid" formalism to address this problem (Berrier et al. 2006) which combines an N-body simulation to account for large-scale structure and the host dark matter halo population and an analytic substructure model (Zentner et al. 2005) to identify satellite galaxies within these host halos.

We examine our samples with the same setup as in Lin et al. (2004) and Lin et al. (2008). They defined close pairs such that the projected separations satisfy $10 h^{-1} kpc \leq \Delta r \leq r_{max}$, where $r_{max} = 30, 50, \text{ or } 100 h^{-1} kpc$, and the rest-frame relative velocity Δv are less than $500 km s^{-1}$. To ensure the selection of the same types of galaxies at different redshifts in the presence of luminosity evolution, a specific range in the evolution-corrected absolute magnitude M_B^e , defined as $M_B + Qz$, was adopted where the evolution is parameterized as $M(z) = M(z=0) - Qz$. Lin et al. (2008) adopted $Q = 1.3$ found by Faber et al. (2007) and restricted the analysis to galaxies with luminosities $-21 \leq M_B^e \leq -19$ for $z = 0.45-1.2$. Applying the mass-to-light ratio in Eq. (6) for B-band with $M_{fid} = 9.9_{-1.3}^{+1.5} \times 10^{11} h^{-1} M_\odot$ and $\beta = 1.5 \pm 0.3$, we are able to convert the mass to the luminosity. The luminosity range, $-21.39 \leq M_B \leq -19.39$, at $z = 0.3$ is considered because the mass-to-light ratio data (Hoekstra et al. 2005) was collected at an average redshift $z \sim 0.3$. The mass range at $z = 0.3$ after conversion is obtained as $2.38 \times 10^{11} h^{-1} M_\odot \leq M \leq 3.78 \times 10^{12} h^{-1} M_\odot$. Moreover, the average number of companions per galaxy is defined as

$$N_c \equiv \frac{2N_p}{N_g}, \quad (14)$$

where N_p is the number density of individual paired galaxies and N_g is the number density of galaxies in the sample as suggested in Berrier et al. (2006). Following Berrier et al. (2006), we also adopt a fiducial relative line-of-sight velocity difference of $|\Delta v| = 500 km s^{-1}$. A close-pair cylinder volume is then constructed by a constant Δv cut. In our analysis, only the $r_{max} = 50$, and $100 h^{-1} kpc$ cases are considered due to the limitation of our mass resolution.

Figure 13 shows the redshift z versus the pair fraction for $r_{max} = 50$ (bottom) and $r_{max} = 100 h^{-1} kpc$ (top). The pair fraction data are taken from Lin et al. (2004) including SSRS2 (da Costa et al. 1998), CNOC2 (Yee et al. 2000), and DEEP2 early data (Davis et al. 2003) and from full samples in Lin et al. (2008) including SRSS2, CNOC2, MGC (Millennium Galaxy Catalog, Liske et al. 2003; Driver et al. 2005; Allen et al. 2006), TKRS (Wirth et al. 2004), and DEEP2 (Davis et al. 2003, 2007). Our data points are consistent with the DEEP2

medium to high redshift observations although at low redshift we have lower values than other observations. However, the mild evolution trend is seen. Using the fitting formula, $N_c(0)(1+z)^m$, proposed in Lin et al. (2004) and Lin et al. (2008), we find the following results. For $r_{max} = 50 h^{-1} kpc$, $N_c(0) = 0.036$ and $m = 1.17$ in the ΛCDM_{100a} , $N_c(0) = 0.074$ and $m = 1.07$ in the ΛCDM_{200} , $N_c(0) = 0.046$ and $m = 0.96$ in the ΛCDM_{100b} , $N_c(0) = 0.025$ and $m = 1.43$ in the ΛCDM_{100c} , and $N_c(0) = 0.028$ and $m = 1.37$ in the $^*\Lambda CDM_{100c}$. For $r_{max} = 100 h^{-1} kpc$, $N_c(0) = 0.137$ and $m = 0.65$ in the ΛCDM_{100a} , $N_c(0) = 0.207$ and $m = 0.95$ in the ΛCDM_{200} , $N_c(0) = 0.182$ and $m = 0.48$ in the ΛCDM_{100b} , $N_c(0) = 0.107$ and $m = 0.98$ in the ΛCDM_{100c} , and $N_c(0) = 0.116$ and $m = 0.92$ in the $^*\Lambda CDM_{100c}$. Apparently, our pair fractions show stronger evolution than those in Lin et al. (2004) and Lin et al. (2008), where $m = 0.51 \pm 0.28$ and $m = 0.41 \pm 0.14$ for $r_{max} = 50 h^{-1} kpc$, and $m = 0.47 \pm 0.18$ and $m = 0.29 \pm 0.05$ for $r_{max} = 100 h^{-1} kpc$, but appear to agree with the results of Berrier et al. (2006) for $r_{max} = 50 h^{-1} kpc$, where $m = 0.42 \pm 0.17$ for V_{now} , the maximum circular velocity that the subhalo has at the current epoch, and $m = 0.99 \pm 0.14$ for V_{in} , the maximum circular velocity that the subhalo had when it was first accreted into the host halo. The results with steeper slope likely can be attributed to insufficient close pairs found at low redshift in our sample. Besides, The apparent difference of N_c appearing in the ΛCDM_{200} is possibly due to the incorrect mass function in the tail at the small mass range of the galactic subhalos.

4. Conclusion and Discussion

In this study we have used the HiFOF method to locate and identify subhalos, and we advocate that galaxies form only in a sufficiently massive halo as a result of high gas cooling efficiency. It is estimated that the threshold halo mass $M_c \approx 4.0 \times 10^{11} h^{-1} M_\odot$ at $z = 0$, and our galaxy samples are constructed from the HiFOF subhalos embedded in the halos satisfying this mass threshold. To test our model, we have analyzed the differential mass function, two-point correlation function (CF), the space density evolution, the HOD, and the pair fraction from our galaxy samples. The results are summarized as follows.

(1) Combing the luminosity function (LF) and the mass to light relation (M/L), a differential mass function can be derived. Based on the lensing signal from Red-Sequence Cluster Survey to determine the galaxy mass, we have corrected the lensing mass in our galaxy samples so as to make fair comparison. We find that the mass functions of our four simulations agree with the LF and M/L data very well.

(2) We compare our galaxy density evolution with the evolution of the observational galaxy number density through the integration of a CF with a proper luminosity cut. Our

simulations basically show fair consistency with observations, except at low-redshift. The insufficient density is likely due to the failure of the assumption at low redshift about the redshift-independent mass-cut. The depletion in the galaxy number density also reflects a similar result in pair fractions found at low-redshift.

(3) We have analyzed CFs of our galaxy subhalos at $z = 0$ and at $z = 1$. At $z = 0$, we select our galaxies for mass $M_g > 4.1 \times 10^{10} h^{-1} M_\odot$ to make comparison with the full flux-limited sample ($14.5 \leq r \leq 17.77$) of SDSS galaxy. Our correlation length r_0 gives $5.50 \pm 0.29 h^{-1} Mpc$, $5.01 \pm 0.12 h^{-1} Mpc$, $6.00 \pm 0.38 h^{-1} Mpc$, and $5.56 \pm 0.19 h^{-1} Mpc$, consistent with $r_0 = 5.59 \pm 0.11 h^{-1} Mpc$ found by the SDSS. As for the power index γ , they are 1.83 ± 0.04 , 1.80 ± 0.02 , 1.76 ± 0.05 , and 1.70 ± 0.02 , comparable to $\gamma = 1.84 \pm 0.01$ given in the SDSS. At $z = 1$, we select samples at $n = 1.3 \times 10^{-2} h^3 Mpc^{-3}$ to setup the same density condition as in the volume-limited sample of bright (corrected), $M_B > -19.0$, DEEP2 galaxies. The projected correlation functions are compared, and our profiles are similar to the one found in DEEP2 galaxies.

(4) We also study r_0 and γ as a function of the space density n . Our galaxies reveal the increase of r_0 as n decreases, a similar result also found in the observation data. In other words, the correlation length r_0 has luminosity dependence, and the brighter the galaxies, the larger the correlation length. On the other hand, the power index γ of observation data displays a nearly constant behavior over a wide range of n at $z = 0$. Despite a smaller values of γ are obtained around $n \approx 10^{-2}$ in our simulations, a roughly constant trend on the whole is seen. The same results are reached at $z = 1$ as well.

(5) We have parameterized our HODs with three parameters M_1 , M_{min} , and α as a function of the galaxy number density. Our values of M_1 and M_{min} and their increasing trend as the galaxy density decreases show good agreement with SDSS data (Zehavi et al. 2005; Zheng et al. 2007) and DEEP2 data (Zheng et al. 2007), and the depletion of the slope α at $z = 0$ may be attributed to insufficient subhalos found in massive clusters.

(6) We have analyzed the kinematic pair fraction of our galaxy samples by selecting the mass in between $2.28 \times 10^{11} h^{-1} M_\odot$ and $3.61 \times 10^{12} h^{-1} M_\odot$ which are obtained by applying the observed mass-to-light ratio to convert the luminosity range $-21.39 \leq M_B^e \leq -19.39$ at $z = 0.3$. Parameterizing the evolution of the pair fraction as $(1+z)^m$, Lin et al. (2008) find that when $r_{max} = 50 h^{-1} kpc$, $m = 0.41 \pm 0.14$ for the full sample. We obtain $m = 1.17$ in ΛCDM_{100a} , $m = 1.07$ in ΛCDM_{200} , $m = 0.96$ in ΛCDM_{100b} , $m = 1.43$ in ΛCDM_{100c} , and $m = 1.37$ in $^* \Lambda CDM_{100c}$. When $r_{max} = 100 h^{-1} kpc$, in contrast to 0.29 ± 0.05 found by Lin et al. (2008), we find $m = 0.65$ in ΛCDM_{100a} , $m = 0.95$ in ΛCDM_{200} , $m = 0.48$ in ΛCDM_{100b} , $m = 0.98$ in ΛCDM_{100c} and $m = 0.92$ in $^* \Lambda CDM_{100c}$. The large deviation at $r_{max} = 50 h^{-1} kpc$ could be explained as insufficient close pairs found in such a short range

at low redshift. However, the situation is less severe for the $r_{max} = 100 h^{-1} kpc$ case where milder evolution trend is seen.

Most of the above tests for our galaxy samples provide supporting evidence for this galaxy model. However, this model has some problems of its own. First, our N-body simulations seem not to have sufficient mass resolution to adequately address the small-scale ($< 50 h^{-1} kpc$) clustering structures, such as the galaxy pair fraction. Second, this model does not provide information of the galaxy morphology. Third, unlike the Millennium simulation (Springel et al. 2005), this model does not contain any empirical ingredient to trace individual galaxy formation and evolution.

The first problem can be circumvented with higher mass-resolution simulations, despite our mass resolution is comparable to the Millennium simulation. The solution to the second problem requires the gas component to be included in the simulation, which can reveal the amount of residual gas angular momentum in the subhalo thereby providing additional information of morphological types. The complexity of the third problem is intractable from the first-principle calculations and it needs an empirical model, much as what was performed to the Millennium, to approximate the physics involved.

Acknowledgements-

We would like to thank Lihwai Lin and Tak-Pong Woo for many helpful discussions and suggestions, and Chia-Hung Jian for his great help in these simulation runs.

REFERENCES

- Allen, P. D., Driver, S. P., Graham, A. W., Cameron, E., Liske, J. & de Propris, R. 2006, MNRAS, **371**, 2
- Bell, E. F., McIntosh, D. H., Katz, N. & Weinberg, M. D. 2003, ApJS, **149**, 289
- Berlind, A. A. et al. 2003, ApJ, **593**, 1
- Berrier, J. C., Bullock, J. S., Barton, E. J., Guenther, H. D., Zentner, A. R., & Wechsler, R. H. 2006, ApJ, **652**, 56
- Blanton, M. R. et al. 2003, ApJ, **592**, 819
- Budavari, T. et al. 2003, ApJ, **595**, 59

- Coil, A. L., Newman, J. A., Cooper, M. C., Davis, M., Faber, S. M., Koo, D. C., & Willmer, C. N. 2006, *ApJ*, **644**, 671
- Conroy, C. et al. 2005, *ApJ*, **635**, 982
- da Costa, L. N. et al. 1998, *AJ*, **116**, 1
- Davis, M., Efstathiou, G., S., Frenk, C. S., & White, S. D. M. 1985, *ApJ*, **292**, 371
- Davis, M. et al. 2003, *SPIE*, **4834**, 161
- Davis, M. et al. 2007, *ApJ*, **660**, L1
- Driver, S. P., Liske, J., Cross, N. J. G., De Propriis, R., & Allen, P. D. 2005, *MNRAS*, **360**, 81
- Faber, S. M. et al. 2007, *ApJ*, **665**, 265
- Gabasch, A. et al. 2004, *A&A*, **412**, 41
- Hoekstra, H., Hsieh, B. C., Yee, H. K. C., Lin, H., & Gladders, M. D. 2005, *ApJ*, **635**, 73
- Ilbert, O. et al. 2005, *A&A*, **439**, 863
- Kitayama, Tetsu, Suto, Yashshi 1996, *ApJ*, **469**, 480
- Klypin, A., GottlAober, S., & Kravsov, A. V. 1999, *ApJ*, **516**, 530
- Kravtsov, A. V., Berlind, A. A., Wechsler, R. H., Klypin, A. A., Gottloeber, S., Allgood, B., & Primack, J. R. 2004, *ApJ*, **609**, 35
- Lin, L. et al. 2004, *ApJ*, **617**, L9
- Lin, L. et al. 2008, *ApJ*, **681**, 232
- Liske, J., Lemon, D. J., Driver, S. P., Cross, N. J. G., & Couch, W. J. 2003, *MNRAS*, **344**, 307
- Neyrinck, M. C., Hamilton, A. J. S., & Gnedin, N. Y. 2004, *MNRAS*, **348**, 1
- Norberg, P. et al. 2002, *MNRAS*, **332**, 827
- Riess, A. G. et al. 1998, *Astron. J.*, **116**, 1009
- Sanchez, A. G., Baugh, C. M., Percival, W. J., Peacock, J. A., Padilla, N. D., Cole, S., Frenk, C. S., & Norberg, P. 2006, *MNRAS*, **336**, 189

- Seljak, U. et al. 2005, Phys. Rev. D, **71**, 103515
- Spergel, D. N. et al. 2003, ApJS, **148**, 175
- Springel, V. 2005, MNRAS, **364**, 1105
- Springel, V. et al. 2005, Nature, **435**, 629
- Springel, V., White, S. D. M., Tormen, G., & KauRmann, G. 2001a, MNRAS, **328**, 726
- Springel, V., Yoshidaa, N., & White, S. D. 2001b, New Astronomy, **6**, 79
- Stadel, J., Katz, N., Weinberg, D. H., & Hernquist, L. 1997, SKID
- Tegmark, M. et al. 2004, ApJ, **606**, 702
- Weinberg, D. H., Dave, R., Katz, N., & Hernquist, L. 2004, ApJ, **601**, 1
- White, S. D. M., Navarro, J. F., Evrard, A. E., & Frenk, C. S. 1993, Nature, **336**, 429
- Wirth, G. D. et al. 2004, AJ, **127**, 3121
- Yee, H. K. C. et al. 2000, ApJS, **129**, 475
- Zehavi, I. et al. 2002, ApJ, **571**, 172
- Zehavi, I. et al. 2005, ApJ, **630**, 1
- Zentner, A. R., Berlind, A. A., Bullock, J. S., Kravtsov, A. V., & Wechsler, R. H. 2005, ApJ, **624**, 505
- Zheng, Z. et al. 2005, ApJ, **633**, 791
- Zheng, Z., Coil, A. L., Zehavi, I. 2007, ApJ, **667**, 760

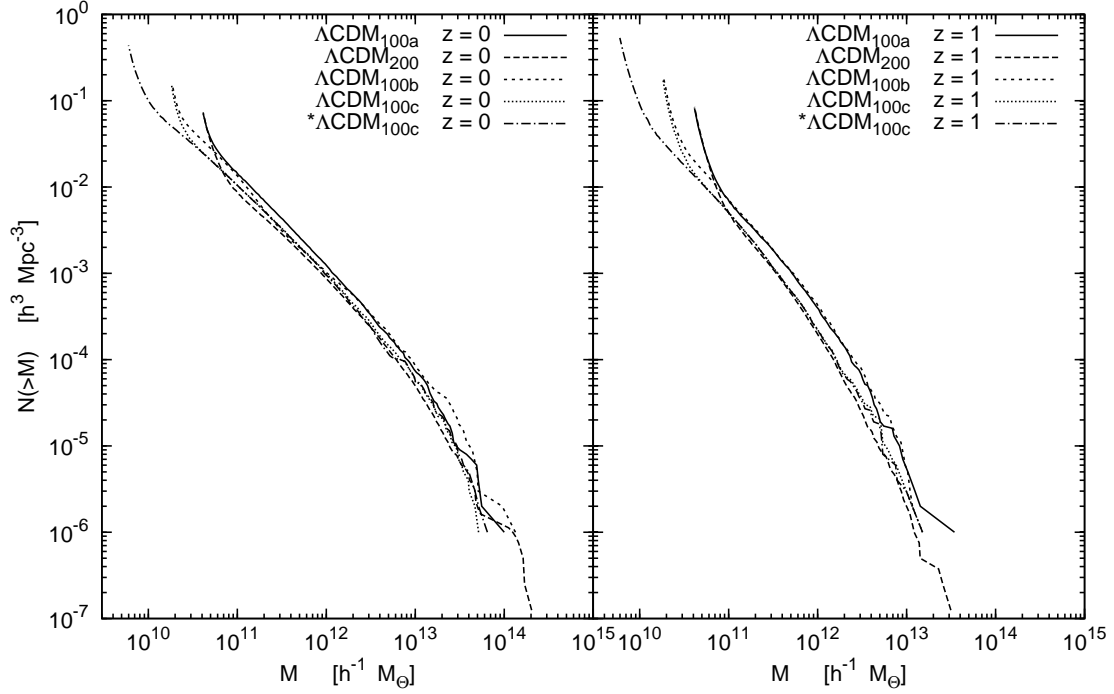


Fig. 2.— The cumulative mass functions of subhalo samples obtained in our analysis at redshift $z = 0$ (left panel) in the ΛCDM_{100a} (solid line), ΛCDM_{200} (long-dashed line), ΛCDM_{100b} (short-dashed line), and ΛCDM_{100c} (dotted line) and at $z = 1$ (right panel). The mass range plotted are down to the minimum mass of $4.1 \times 10^{10} h^{-1} M_{\odot}$ in the ΛCDM_{100a} and ΛCDM_{200} , to that of $1.9 \times 10^{10} h^{-1} M_{\odot}$ in the ΛCDM_{100b} , to that of $1.52 \times 10^{10} h^{-1} M_{\odot}$ in the ΛCDM_{100c} , and to that of $5.16 \times 10^9 h^{-1} M_{\odot}$ in the $*\Lambda\text{CDM}_{100c}$. These mass functions are generally consistent with each other. As a result, it is inferred that the influence of the box size and resolution effect are not important for our HiFOF samples.

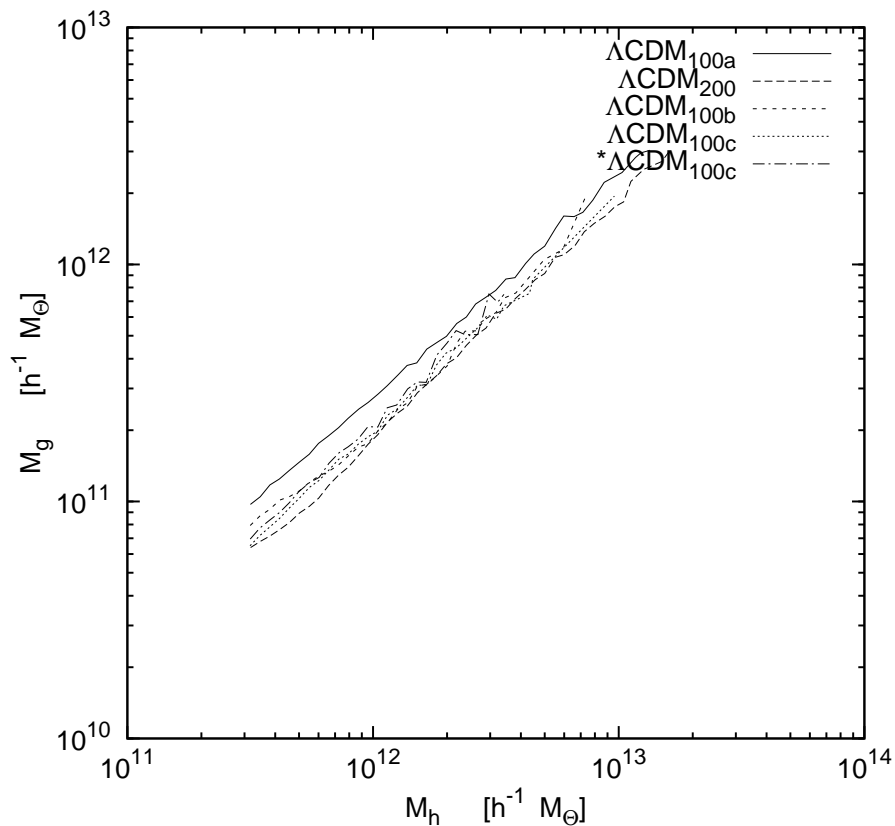


Fig. 3.— The diagram shows M_h (Mass of the isolated FOF halos) vs. M_g (Mass of the HiFOF identified subhalos) at redshift $z \sim 0.3$. As shown in the figure, the relation can be approximated as a power law. This power law is used to give a correction on galaxy mass when our galaxy samples are compared with the observation in Hoekstra et al. (2005).

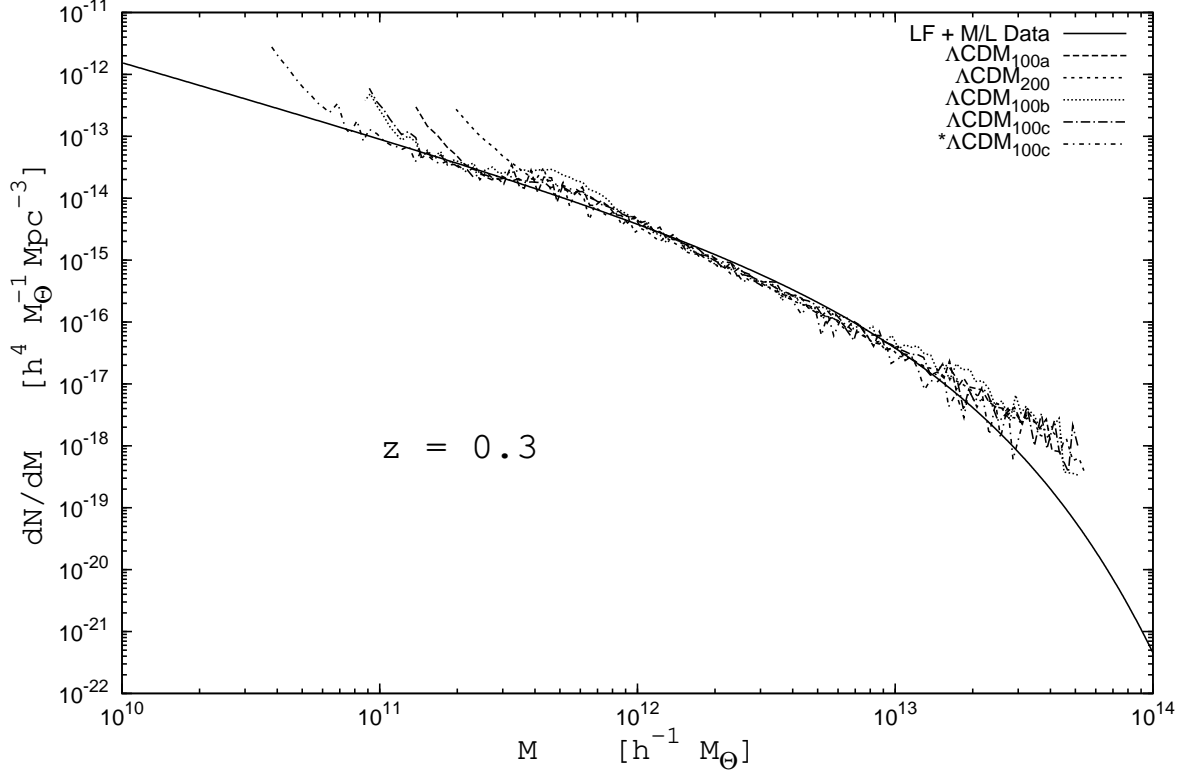


Fig. 4.— Differential mass functions at redshift $z = 0.3$ of LF + M/L data (solid line), the ΛCDM_{100a} samples (long-dashed line), ΛCDM_{200} (short-dashed line), ΛCDM_{100b} (dotted line), ΛCDM_{100c} (dashed-dotted line), and $^*\Lambda\text{CDM}_{100c}$ (short-dashed dotted line). The mass of our galaxy samples is modified according to the relation in Fig 3. We list the space density as follows. The number density $n = 2.01 \times 10^{-2} h^3 \text{ Mpc}^{-3}$ in ΛCDM_{100a} , $2.11 \times 10^{-2} h^3 \text{ Mpc}^{-3}$ in ΛCDM_{200} , $3.22 \times 10^{-2} h^3 \text{ Mpc}^{-3}$ in ΛCDM_{100b} , $2.82 \times 10^{-2} h^3 \text{ Mpc}^{-3}$ in ΛCDM_{100c} , and $4.77 \times 10^{-2} h^3 \text{ Mpc}^{-3}$ in $^*\Lambda\text{CDM}_{100c}$. Our data profiles are similar to the observational data line despite deviations shown in the two ends, the lower and higher mass range.

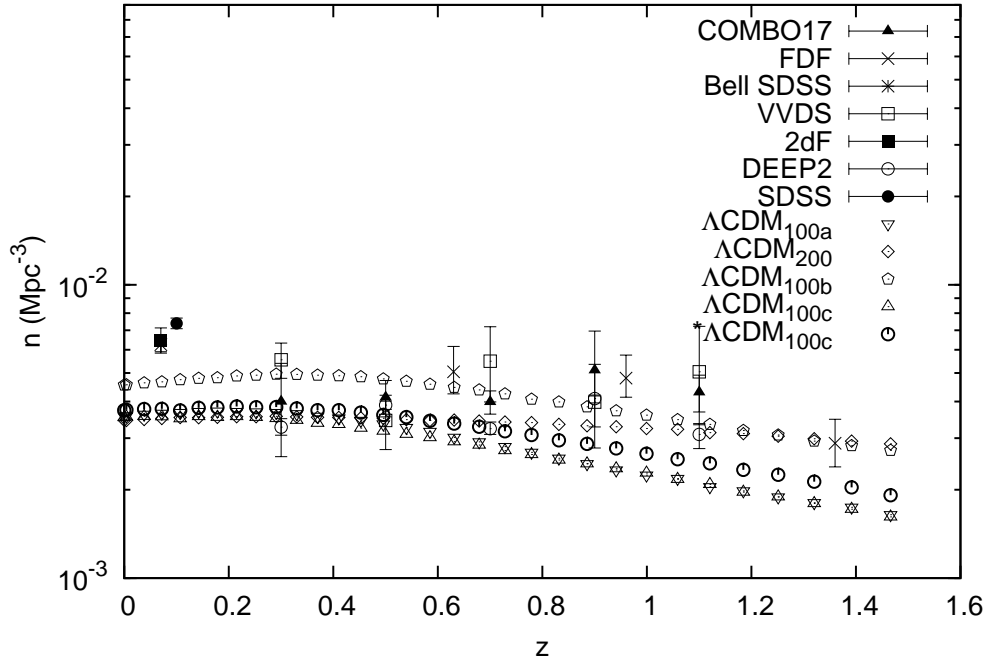


Fig. 5.— Galaxy density as a function of the redshift is plotted. Observational data are based on the data of the LFs in Faber et al. (2007) and can be converted to the galaxy density evolution by using Eq. (8). A proper luminosity cut, $L \geq L_*(z)/4$, is adopted for the density calculation, and combining the data of the DEEP2 B-band galaxies and the mass-to-light relation at $z \sim 0.3$, as well as the $M_g - M_h$ relation, a corresponding mass-cut can be obtained and then applied to galaxy samples at other redshifts to get $n(z)$.

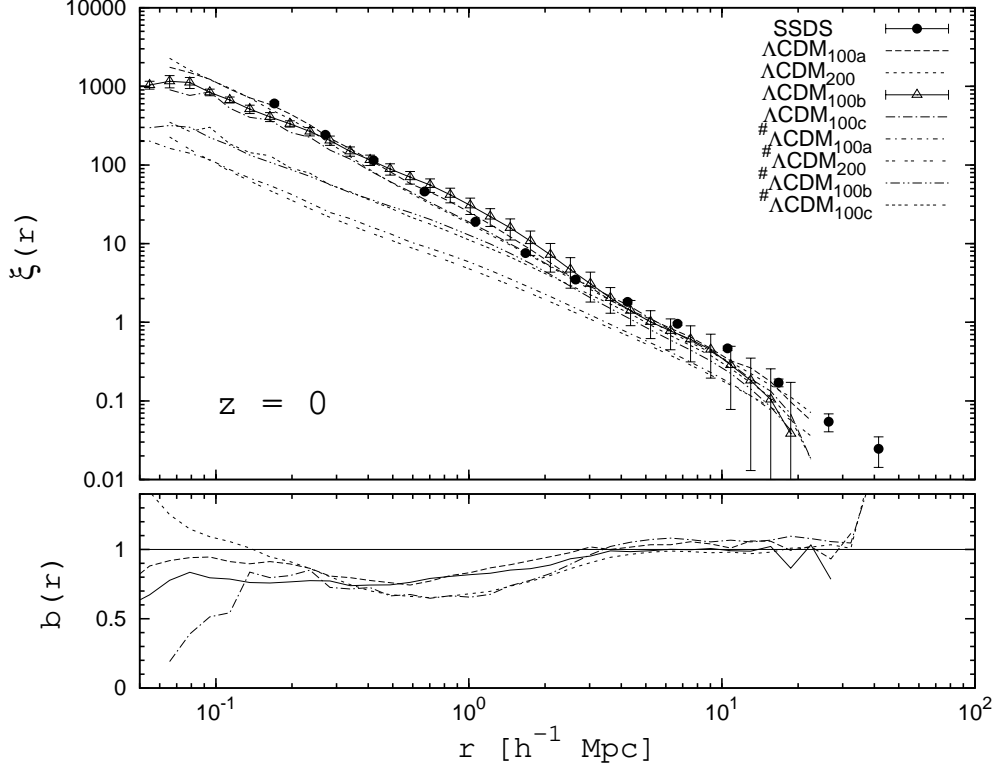


Fig. 6.— Top: Correlation functions of the galaxy samples at $z = 0$ in the ΛCDM_{100a} (dashed line), ΛCDM_{200} (dotted line), ΛCDM_{100b} (open triangle with the error bar), and ΛCDM_{100c} (dashed-dotted line) are compared with the correlation function of the full flux-limited sample ($14.5 \leq r \leq 17.77$) of the SDSS galaxy (Zehavi et al. 2005). In addition, the subhalo subhalo correlation ξ_{hh} is presented with $\#$. We further take a galaxy mass-cut, $M_g \geq 4.1 \times 10^{10} h^{-1} M_\odot$, on ΛCDM_{100b} and ΛCDM_{100c} in order to make a correct comparison with ΛCDM_{100a} and ΛCDM_{200} . It can be seen that the four simulations are all very close the observational data. The error bars in our samples indicate the "jackknife" 1σ errors, computed using the eight octants of the simulation cube. Bottom: The bias $b(r)$, defined as $(\xi_{gg}(r)/\xi_{mm}(r))^{1/2}$, as a function of the correlation length, where $\xi_{gg}(r)$ and $\xi_{mm}(r)$ represent the galaxy-galaxy correlation function and the dark matter dark matter correlation function, respectively. Four simulations reveal similar profiles and roughly the same number densities. The deviation of the bias values at $r < 1 h^{-1} \text{ Mpc}$ are probably from the different softening-length adoption as well as from sample variance.

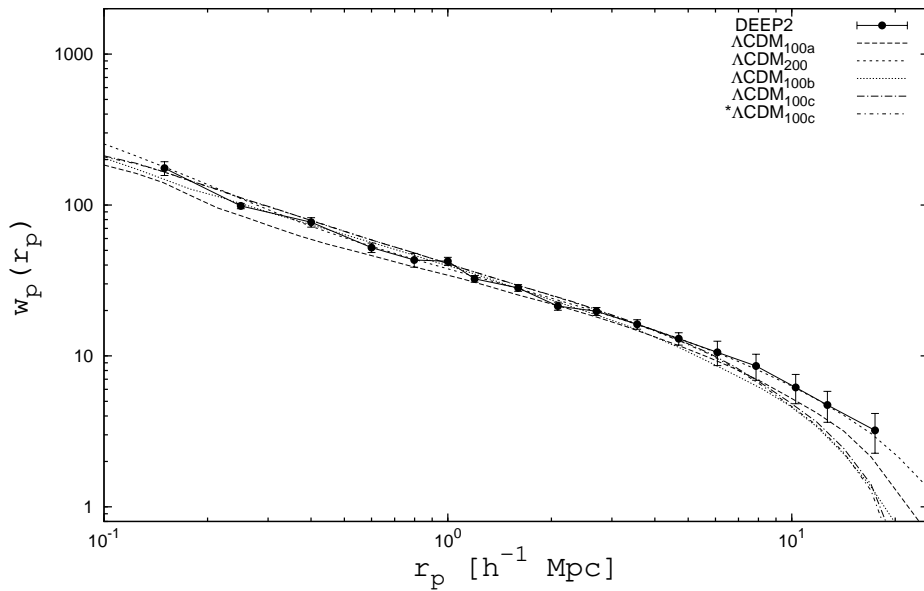


Fig. 7.— A comparison of the projected correlation functions between our four simulations at $z = 1$ and the DEEP2 volume limited data of bright, $M_B < -19.0$, galaxies (Coil et al. 2006). The CF of the DEEP2 data has a density $0.013 h^3 Mpc^{-3}$. We therefore select our samples to have the same density, and the results can be found to be in good agreement with the DEEP2 data.

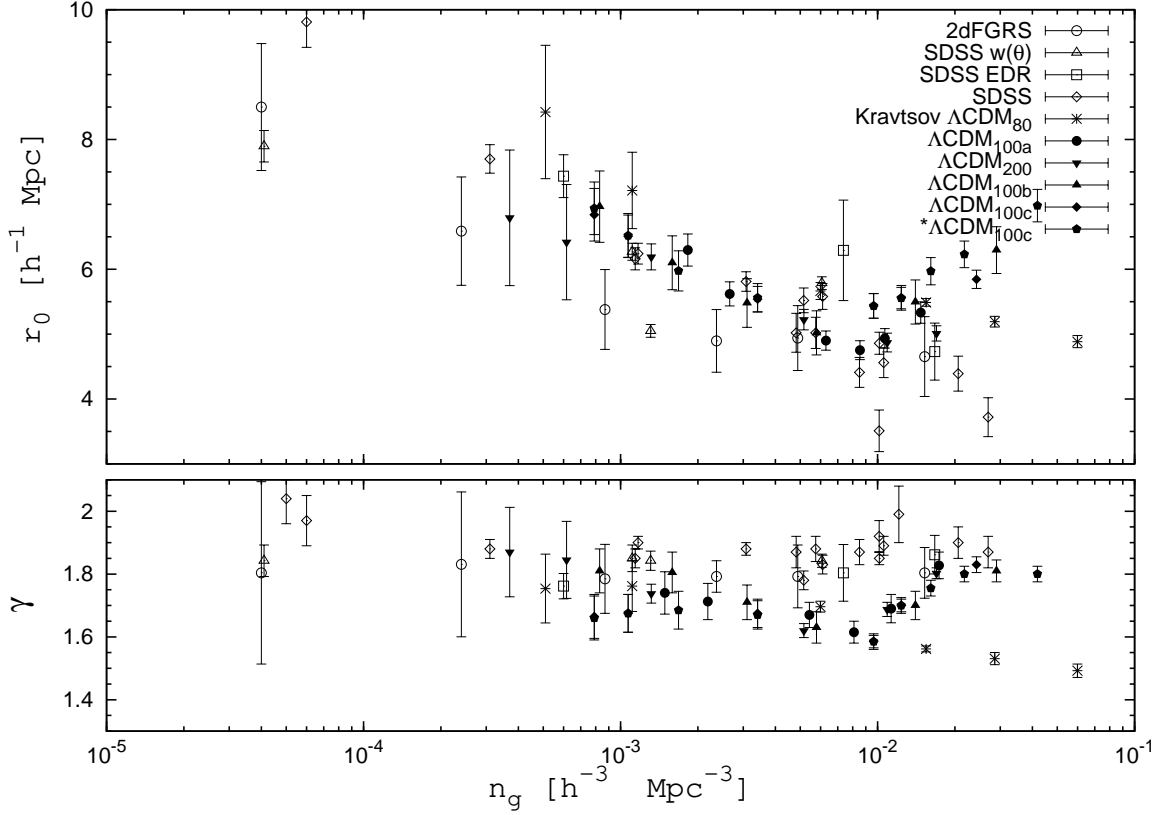


Fig. 8.— Top: Best-fit correlation scale r_0 as a function of number density at the present-day epoch. Bottom: Best-fit slope γ of the correlation function as a function of number density. This plot is based on the Fig. 11 in Kravtsov et al. (2004) plus the newest SDSS data (Zehavi et al. 2005) and our data. Our values of the correlation length r_0 are consistent with observational data. The values of the power index γ are lower at density around $n = 10^{-2} h^3 Mpc^{-3}$. However, the agreement between observations and our data is seen.

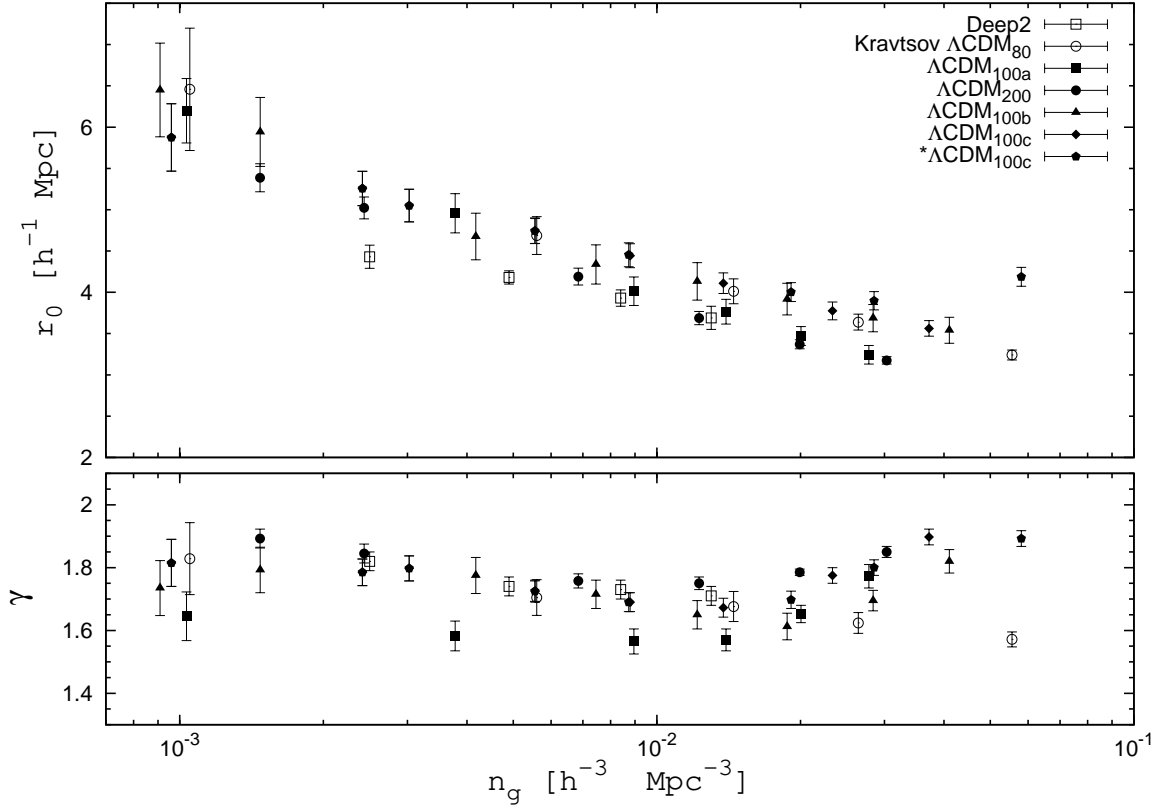


Fig. 9.— Same as Fig. 8, but for $z = 1$. We additionally include DEEP2 data released by (Coil et al. 2006) as well as our data. It is found that the correlation length and the power index in our simulations match DEEP2 data well.

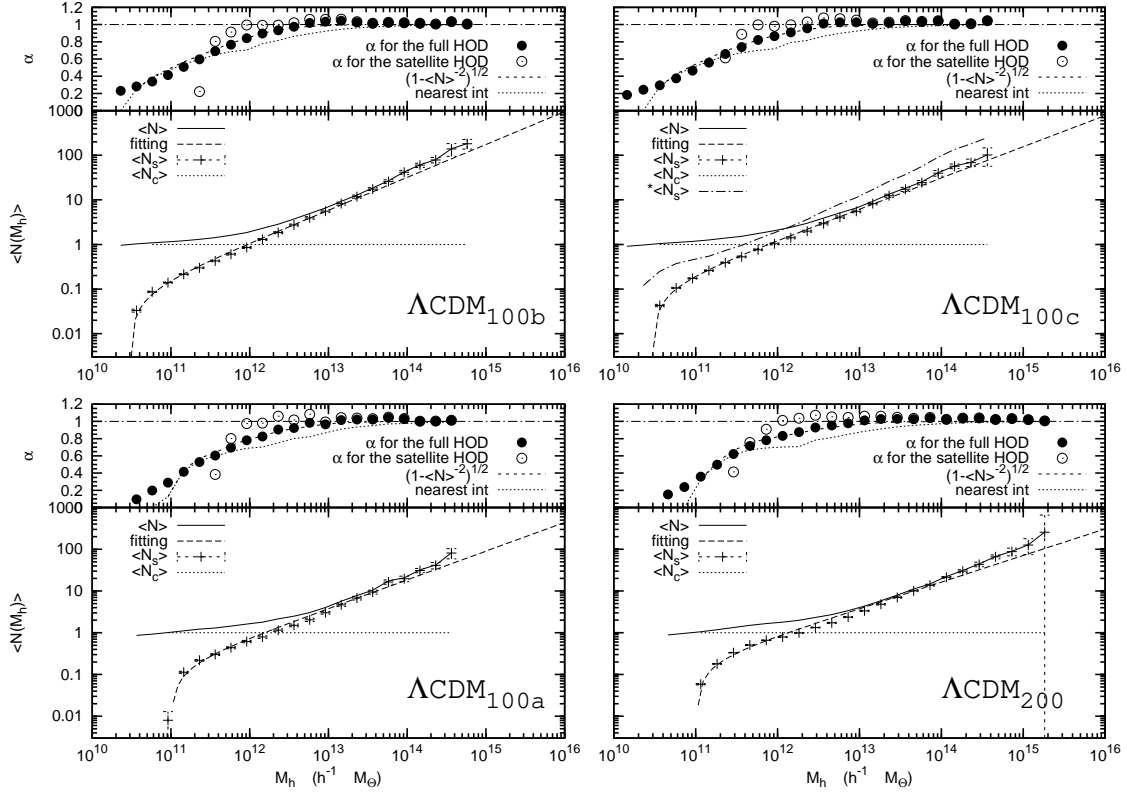


Fig. 10.— The four panels from left to right and from top to bottom are the HODs from the ΛCDM_{100b} , the ΛCDM_{100c} , the ΛCDM_{100a} , and the ΛCDM_{200} , respectively. Top: Parameter $\alpha \equiv \langle N(N - 1) \rangle^{1/2} / \langle N \rangle$ is a convenient measure of how different $P(N|M)$ is from the Poisson distribution. The dot points are for the full HOD, the open points are for the satellite HOD, the dashed line is for $(1 - 1/\langle N \rangle^2)^{1/2}$, and the dotted line is for the nearest integer distribution. It could be observed that the HOD of satellites remains close to Poisson ($\alpha = 1$) down to masses much smaller than for the full HOD. At small M_h the nearest integer distribution could well describe the full HOD (dotted line). Bottom: The first moments of Halo Occupation Distribution (HOD) at $z = 0$ for the ΛCDM_{100b} simulation the number density $n = 1.53 \times 10^{-1} h^3 \text{ Mpc}^{-3}$, for the ΛCDM_{100c} simulation the number density $n = 1.53 \times 10^{-1} h^3 \text{ Mpc}^{-3}$, the ΛCDM_{100a} simulation the number density $n = 7.11 \times 10^{-2} h^3 \text{ Mpc}^{-3}$, and for the ΛCDM_{200} simulation the number density $n = 7.33 \times 10^{-2} h^3 \text{ Mpc}^{-3}$. In ΛCDM_{100c} , $\langle N_s \rangle$ additionally includes the $n_{\min} = 10$ case corresponding to $5.16 \times 10^9 h^{-1} M_\odot$ with $n = 4.37 \times 10^{-1} h^3 \text{ Mpc}^{-3}$. The solid line represents the mean total number of halos including hosts, the + points show the data of the mean number of satellite halos, and the dashed line gives the fitting line using Eq. (13). The error bar of the + point is the uncertainty in the mean.

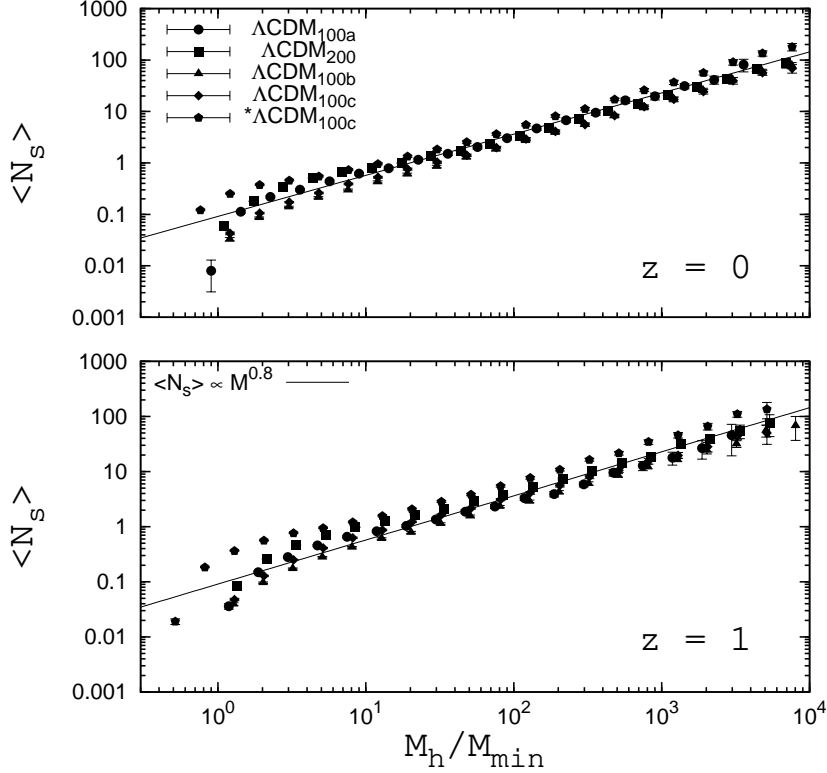


Fig. 11.— Mean number of subhalos $\langle N_s \rangle$ as a function of host halo mass in unit of M_{min} for the samples in ΛCDM_{100a} (filled circles), in ΛCDM_{200} (filled squares), in ΛCDM_{100b} (filled triangles), in ΛCDM_{100c} (filled diamond), and $^*\Lambda\text{CDM}_{100c}$ (filled pentagon) at $z = 0$ (top) and at $z = 1$ (bottom). The dotted line represents the linear relation $\langle N_s \rangle \propto M_h^{0.8}$. From the plot, it is seen that the effect of different box sizes, the mass resolution and the different number densities have little influence on the satellite HOD. In addition, the evolution of $\langle N_s \rangle$ with time is weak when we compare two redshifts.

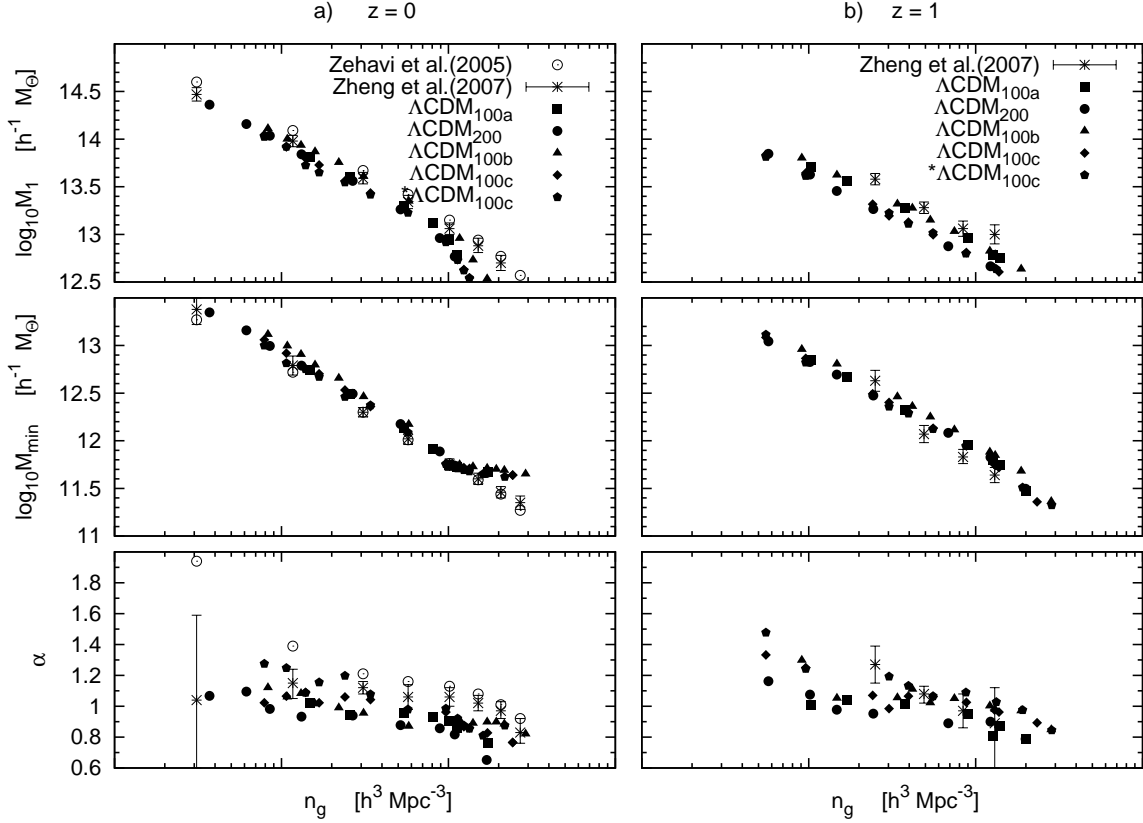


Fig. 12.— From top to bottom, the three fitting parameters M_1 , M_{min} , and α of the HOD formulation are plotted as a function of the galaxy number density n_g . In 12(a), the open circles represent SDSS data (Zehavi et al. 2005) and the stars with errorbars give also SDSS data (Zheng et al. 2007), and in 12(b) the stars with errorbars give DEEP2 data (Zheng et al. 2007), while the filled square, circle, triangle, diamond, and pentagon are for the ΛCDM_{100a} , ΛCDM_{200} , ΛCDM_{100b} , ΛCDM_{100c} , and $^*\Lambda\text{CDM}_{100c}$ data. Consistencies between SDSS galaxies and our galaxy samples can be observed at $z = 0$. The good agreements are also seen between DEEP2 galaxies and ours at $z = 1$.

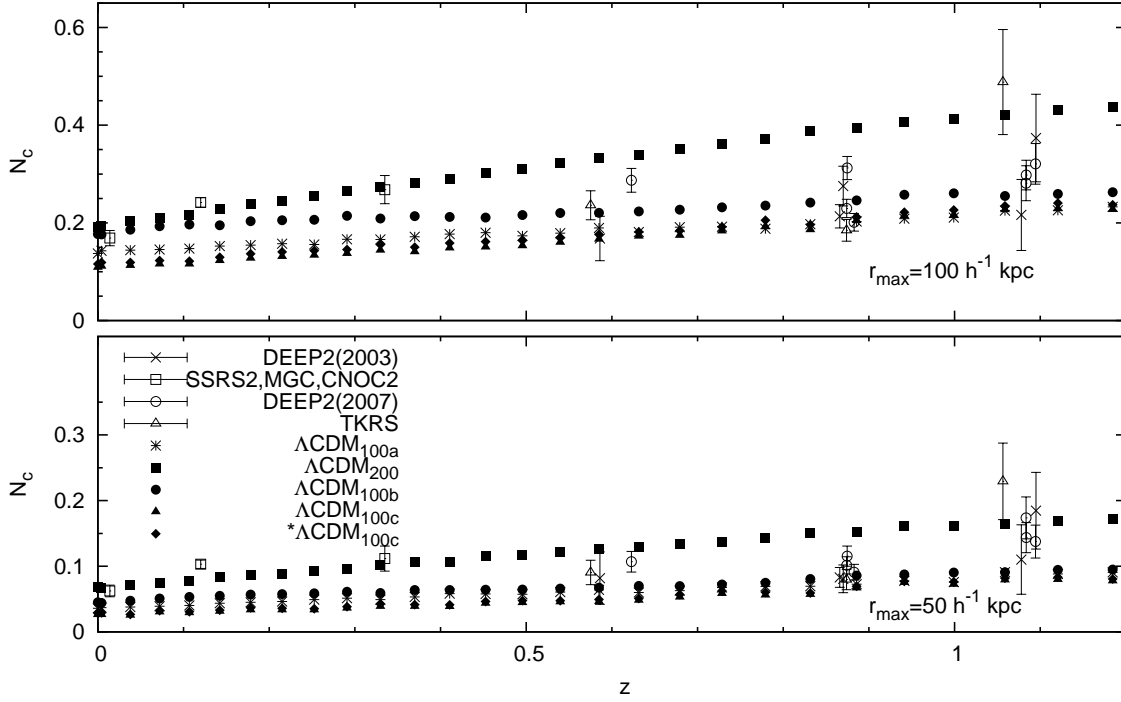


Fig. 13.— Pair fraction, N_c , as a function of redshift z . The crosses mark the results from DEEP2 early data (2003). The open squares represents measurements from SSRS2, MGC, and CNOC2. The open circles show DEEP2 data (2007). The open triangles are from TKRS. The stars, filled squares, circles, triangles, and diamonds give our simulation results from ΛCDM_{100a} , ΛCDM_{200} , ΛCDM_{100b} , ΛCDM_{100c} , and $*\Lambda\text{CDM}_{100c}$. Two cases of r_{\max} , 50 (bottom) and 100 (top) $h^{-1} \text{ kpc}$, are considered.

Table 1: Simulation Parameters

Name	L_{Box} ($h^{-1} Mpc$)	N_{dm}	M_{dm} ($h^{-1} M_{\odot}$)	$\epsilon_{z=0}$ ($h^{-1} kpc$)	σ_8
ΛCDM_{100a}	100	256^3	4.125×10^9	6.0	0.94
ΛCDM_{200}	200	512^3	4.125×10^9	10.0	0.94
ΛCDM_{100b}	100	512^3	6.188×10^8	3.0	0.94
ΛCDM_{100c}	100	512^3	5.156×10^8	10.0	0.94

Table 2: Fit Parameters for $\langle N_s \rangle$ Fitting Function

Name	M_1^a	β	C	M_{min}^b
$z = 0 :$				
ΛCDM_{100a}	1.44 ± 0.14	0.688 ± 0.04	0.071 ± 0.001	10.1
ΛCDM_{200}	1.25 ± 0.11	0.638 ± 0.03	0.084 ± 0.001	10.5
ΛCDM_{100b}	0.91 ± 0.04	0.737 ± 0.02	0.033 ± 0.003	3.03
ΛCDM_{100c}	0.74 ± 0.04	0.700 ± 0.02	0.041 ± 0.003	5.13
$z = 1 :$				
ΛCDM_{100a}	1.20 ± 0.08	0.68 ± 0.04	0.065 ± 0.001	7.76
ΛCDM_{200}	0.75 ± 0.04	0.66 ± 0.03	0.122 ± 0.001	9.08
ΛCDM_{100b}	0.72 ± 0.01	0.72 ± 0.01	0.039 ± 0.001	2.86
ΛCDM_{100c}	0.46 ± 0.02	0.72 ± 0.02	0.062 ± 0.003	2.82

^a M_1 in unit of $10^{12} h^{-1} M_{\odot}$

^b M_{min} in unit of $10^{10} h^{-1} M_{\odot}$

Note. — Fitting Formula : $\langle N_s \rangle = \left(\frac{M}{M_1} - C \right)^{\beta}$